


## PAPER



Cite this: *J. Mater. Chem. A*, 2025, **13**, 3064

# Porous polymer in polymer structure created using carbon dots for high-performance gel polymer electrolytes†

Zun-Hui Huang, Hao-Wen Sun, Tian-Bing Song, Jia-Wen Ni and Huan-Ming Xiong \*

A new polymer in polymer structure was constructed, incorporating two distinct polymers: the rigid PVDF–HFP as the porous framework and the flexible PEO, which served both as the filler and the liquid electrolyte absorber. For the first time, the polymeric porous structure was engineered using CDs, which could be recycled through washing and reused in subsequent pore creation processes. The high porosity and robust structure of the PVDF–HFP framework ensured effective deposition of PEO and absorption of the electrolyte. The resulting gel polymer electrolytes (GPEs) exhibited excellent conductivity, a wide electrochemical stability window, and considerable lithium-ion transference numbers at room temperature. These GPEs were employed in lithium metal batteries (LMBs), which exhibited exceptional cycling stability exceeding 3000 h, high rate capability, and a coulombic efficiency of nearly 100%. Both SEM and XPS investigations of lithium anodes dismantled from LMBs after extended cycling revealed the formation of stable solid-electrolyte interphase (SEI) layers on the lithium surface, which effectively hindered dendrite growth and minimized anode corrosion. This research offers a solution for fabricating high-performance GPEs for LMBs with long cycle lifespans while also introducing a new technique for preparing porous polymer materials using CDs.

Received 27th September 2024  
Accepted 5th December 2024

DOI: 10.1039/d4ta06893a

rsc.li/materials-a

## 1 Introduction

Lithium metal batteries (LMBs) have received extensive research interest in recent years owing to their use of lithium metal anodes, which offer a high theoretical capacity, low electrochemical potential, and the lowest density among all metals.<sup>1</sup> However, conventional liquid electrolytes (LEs) used in Li-ion batteries are incompatible with lithium metal anodes, as they undergo unfavorable reactions and produce unstable by-products. This issue becomes particularly problematic during charge–discharge cycles, where the formation of lithium dendrites and the accumulation of “dead lithium” compromise both the safety and capacity of LMBs.<sup>2</sup> In order to overcome these challenges, numerous strategies have been proposed, such as electrolyte modification,<sup>3</sup> solid-electrolyte interphase (SEI) layer construction,<sup>4</sup> and the development of novel electrolytes.<sup>5</sup> Among new electrolyte types, SPEs, which are solvent-free, demonstrate excellent flexibility for mechanical processing and favorable interfacial stability when in contact with Li metal.<sup>6–8</sup> However, the ionic conductivity of SPEs at room

temperature remains too low, necessitating operation of LMBs at temperatures above 60 °C.<sup>9</sup> As a balanced alternative to both SPEs and LEs, GPEs exhibit moderate ionic conductivity at room temperature, low interfacial impedance, and ease of scalability, making them widely adopted in the battery industry.<sup>10</sup>

GPEs are typically formed by incorporating LEs or plasticizers into polymeric hosts.<sup>11</sup> The liquid solvents and salts are bound by the polymeric groups, which also restrict the migration of Li<sup>+</sup> ions, thereby influencing the ionic conductivity of GPEs. The electrolyte retention rate in GPEs profoundly impacts overall electrochemical performance, and it can be enhanced by increasing the porosity or introducing ether-based polymers. However, these improvements often come at the expense of the mechanical properties of the GPEs.<sup>12,13</sup> To simultaneously achieve both good mechanical properties and high ionic conductivities in GPEs, a “polymer in polymer” structure has been proposed recently. This structure involves the infiltration of highly conductive polymer electrolytes into well-designed porous rigid polymer frameworks.<sup>14,15</sup> Such porous frameworks have been prepared using laser etching,<sup>16</sup> electrospinning,<sup>17</sup> calcination,<sup>18</sup> solvent exchange,<sup>19</sup> acid etching<sup>20</sup> and other tailored methodologies.<sup>21</sup> These techniques depend on sophisticated equipment and stringent experimental conditions that limit their practical applications.

Carbon dots (CDs), a new type of nanomaterials with large specific surface area and multiple functions,<sup>22,23</sup> are often used

Department of Chemistry and Shanghai Key Laboratory of Molecular Catalysis and Innovative Materials, Fudan University, Shanghai 200433, P. R. China. E-mail: hmxiong@fudan.edu.cn

† Electronic supplementary information (ESI) available. See DOI: <https://doi.org/10.1039/d4ta06893a>

to modify electrode materials<sup>24</sup> and electrolyte additives to regulate the uniform deposition and construct an SEI protection layer.<sup>25–28</sup> In the present work, a simple method is suggested to prepare pores in the polymer frameworks, in which carbon dots (CDs) are dispersed homogeneously in the host polymer by dissolving and casting, and then extracted using another solvent. The host polymer is the famous PVDF–HFP (polyvinylidene fluoride–hexafluoropropylene copolymer) which has excellent stability, high dielectric constant, and good mechanical strength.<sup>20,21</sup> Afterwards, the guest polymer PEO (polyethylene oxide) is introduced to form numerous pores in PVDF–HFP for absorbing LEs to form GPEs, because PEO is known for its high polarity and ability to absorb electrolytes.<sup>29</sup> Moreover, the introduction process of PEO, soaking and freeze-drying, can improve the porosity and connectivity of the porous structure. As a result, such a “PEO in PVDF–HFP” structure has a reduced interfacial impedance and a robust mechanical strength simultaneously.

## 2 Experimental section

### 2.1 Materials

Citric acid (Sinopharm Group, 99%), ethylenediamine (Sinopharm Group, AR) were used directly. *N,N*-Dimethylformamide (DMF, AR) and *N*-methyl-2-pyrrolidone (NMP, 99.5%) were used as solvents. LiFePO<sub>4</sub> and lithium disc were supplied by Kluthe Chemical (Shanghai) Co., Ltd. Polyvinylidene fluoride and hexafluoropropylene (PVDF–HFP) and polyethylene oxide (PEO) were supplied from Shanghai Chunai Biotechnology Co., Ltd (China). Liquid electrolytes (1 M LiPF<sub>6</sub>, EC/DEC/EMC = 1/1/1 v/v) were purchased from Nanjing Mojes Technology Energy Co., Ltd (China).

### 2.2 Synthesizing carbon dots (CDs)

Carbon dots (CDs) were synthesized using a solvothermal method, in which 2.89 g of citric acid and 1 mL of ethylenediamine were dissolved in 5 mL of DMF solution taken in an autoclave, which was then heated at 180 °C for 5 h. The obtained products were naturally cooled to room temperature and added to a beaker containing 100 mL of ethanol solution. The CDs precipitated in the ethanol solution and were then centrifuged at a speed of 4000 rpm for 5 min to obtain brown CDs. After pouring out the supernatant of the centrifuge tube, the precipitated CDs were washed with ethanol three times to remove the residual solvents, followed by drying in an oven at 80 °C.

### 2.3 Preparing GPE

0.6 g of CDs were dissolved in 10 mL of DMF solution (named CD-DMF) for use. PVDF–HFP (Sigma-Aldrich, average molar mass = 600 000 g mol<sup>-1</sup>) and CD-DMF were mixed in different mass ratios of 0 : 1, 0.25 : 1, 0.5 : 1, 0.75 : 1, 1 : 1 and 1.25 : 1, respectively, in 10 g of NMP (*N*-methyl-2-pyrrolidone), and stirred overnight to obtain homogenous solutions. The obtained solutions were placed into a polytetrafluoroethylene mold and heated in an oven at 60 °C for 2 h to remove NMP.

Deionized water was then dropped into the mold to solidify the PVDF–HFP film. Further, to remove CDs, the polymer films were immersed in the boiling water. 0.5 g of PEO (Shanghai Pureone Biological Co., Ltd, average molar mass = 1 000 000 g mol<sup>-1</sup>) was dissolved in 100 mL of water to obtain a PEO aqueous solution. The as-treated polymer films were soaked in a PEO aqueous solution, and ultrasonicated to make the PEO solution infiltrate into the pores of the film. Then, the obtained film was placed into a refrigerator at 0 °C overnight. In this process, the ice would expand the pores and pierce through the polymer film, thus forming three-dimensional channels in the film. Afterwards, the frozen film was placed in a freeze dryer for 48 h of drying to completely remove the water. By controlling the content of the added CDs, the porous films with different morphologies were obtained, named CD-PPM-PEO (carbon dot-induced porous polymer membranes). The PVDF–HFP/PEO mixed film was made in the same way without CDs and was named PPM-PEO.

In terms of the liquid electrolyte absorbed by CD-PPM, ethylene carbonate (EC), ethyl methyl carbonate (EMC), and dimethyl carbonate (DMC) with a mass ratio of 1 : 1 : 1 were used as solvents, and LiPF<sub>6</sub> was selected for lithium salt with the concentration of 1 M. The CD-PPM-PEO and PPM-PEO were cut into a circle shape and immersed in an electrolyte to form the gel polymer electrolyte.

### 2.4 Preparing electrodes and the cell assembly

To obtain the required positive electrode, LiFePO<sub>4</sub>, carbon black and PVDF were dispersed in NMP with a weight ratio of 8 : 1 : 1. After magnetically stirring for 8 h to obtain a uniform slurry, the obtained slurry was coated onto aluminum foils and dried at 60 °C overnight in an oven. Then, the dried electrode was transferred to a vacuum oven and treated at 120 °C for 2 days to remove residual NMP. The obtained electrode was cut into discs with a diameter of 16 mm, packed with lithium metal sheets, and PCCes into a battery, and transferred in an argon-filled glove box (H<sub>2</sub>O, O<sub>2</sub> < 0.01 ppm). The galvanostatic charge/discharge cycling tests for Li||Li symmetric batteries were measured at 0.1 and 0.5 mA cm<sup>-2</sup> with an interval of 1 h. The cycle test was carried out at a rate of 0.5C to Li||LiFePO<sub>4</sub> (1C = 170 mA h g<sup>-1</sup>).

### 2.5 Characterization

The X-ray diffraction (XRD) patterns were collected using a Bruker D4 Endeavor X-ray diffractometer with Cu-Kα radiation ( $\lambda = 0.1541$  nm, 40 kV). Fourier transform infrared (FTIR) spectra were recorded on a PerkinElmer Avatar 360 E. S. P. FTIR spectrometer in a range of 4000–400 cm<sup>-1</sup> by using the KBr pellet method. X-ray photoelectron spectroscopic (XPS) data were obtained on a Thermo ESCALAB 250 electron spectrometer using an Al-Kα X-ray source (1486.6 eV). The morphologies of the samples were characterized by scanning electron microscopy (SEM) under a JSM-6390 microscope, while the transmission electron microscope (TEM) images of the samples were obtained using a high-resolution transmission electron microscope (JEM-2010) at 200 kV.

## 2.6 Electrochemical measurements

Three kinds of symmetric SS (stainless steel) cells employing different electrolytes, SS||PCCES||SS, SS||PVDF||SS, and SS||LEs||SS were assembled to test the ionic conductivities using the following equation.

$$\sigma = L/RS$$

$L$ ,  $R$ , and  $S$  are the thickness, the bulk resistance, and the area of the electrolyte, respectively. The thickness of the PCCES is about 200  $\mu\text{m}$ , and their diameter is 12 mm. The impedance spectrum is operated in the range of 0.1–100 kHz while 10 mV of the amplitude voltage was applied.

Cyclic voltammetry (CV) at a scan rate of 0.5  $\text{mV s}^{-1}$  was performed to determine the electrochemical windows of the GPEs in SS||PCCES||Li batteries. Symmetric Li||Li batteries were assembled to test ion transference number ( $t_{\text{Li}^+}$ ) by combining impedance spectra and chronoamperometry. The value of the  $t_{\text{Li}^+}$  was calculated using the following equation.

$$t_{\text{Li}^+} = (I_s(V - I_0R_0))/(I_0(V - I_sR_s))$$

$V$  is the amplitude voltage, and  $I_0$  and  $R_0$  are the initial current and charge transfer resistance, respectively.  $I_s$  and  $R_s$  are steady-state parts after DC polarization, respectively.

## 3 Results and discussion

### 3.1 Preparation of PEO-CD-PPM

The synthesis of CDs was performed by employing citric acid and ethylenediamine as precursors,<sup>23</sup> and DMF ( $N,N$ -

dimethylformamide) as the solvent. The solution was placed in a PTFE-lined autoclave for a solvothermal reaction at 180  $^\circ\text{C}$  for 5 h (Fig. S1†). The as-prepared CDs were precipitated, washed and dried, and their weight was about several grams from an autoclave of volume 100 mL. Such a high yield ensured the performance of subsequent experiments. TEM (transmission electron microscopy) images confirmed the products are monodispersed CDs less than 10 nm. FTIR (Fourier-transform infrared spectroscopy) spectra show that CDs have various surface groups, including  $-\text{OH}$  ( $\sim 3400 \text{ cm}^{-1}$ ),  $\text{C}=\text{O}$  ( $1700 \text{ cm}^{-1}$ ),<sup>30</sup>  $-\text{NH}_2$  ( $3000\text{--}3500 \text{ cm}^{-1}$ ),<sup>31</sup> and  $\text{C}-\text{O}-\text{C}$  ( $1100 \text{ cm}^{-1}$ ).<sup>32</sup> These groups endow CDs with good dispersion in many solvents, such as DMF, water, and NMP.<sup>33</sup> For the first time, CDs were used as pore-forming agents to prepare porous polymer membranes. Fig. 1 illustrates the manufacturing process of such CD-derived porous polymer membranes (CD-PPMs). Appropriate amounts of CD-DMF solution (containing CDs of  $60 \text{ mg mL}^{-1}$ ) and PVDF-HFP powder were dissolved in NMP, followed by heating to form a gel. The gel was immersed in boiling water to remove CDs and solvents thoroughly, and the resulting PVDF-HFP membrane was full of pores. Fig. S2† presents the SEM images of the above PVDF-HFP membrane derived from different weight ratios of PVDF-HFP and CD-DMF. Obviously, when no CDs are used, the obtained PVDF-HFP film is solid with few pores (designated as PPM as a control). When more and more CDs are involved in making the pores, both the porosity and the pore size increase gradually in the resulting CD-PPM films. Although PEO can be used as an additive to manipulate the pore morphology within PVDF-HFP,<sup>34</sup> blending PEO with other polymers directly will compromise the mechanical integrity of the as-prepared GPE membranes.<sup>35</sup> Therefore, our present research suggests a new route, *i.e.*, filling

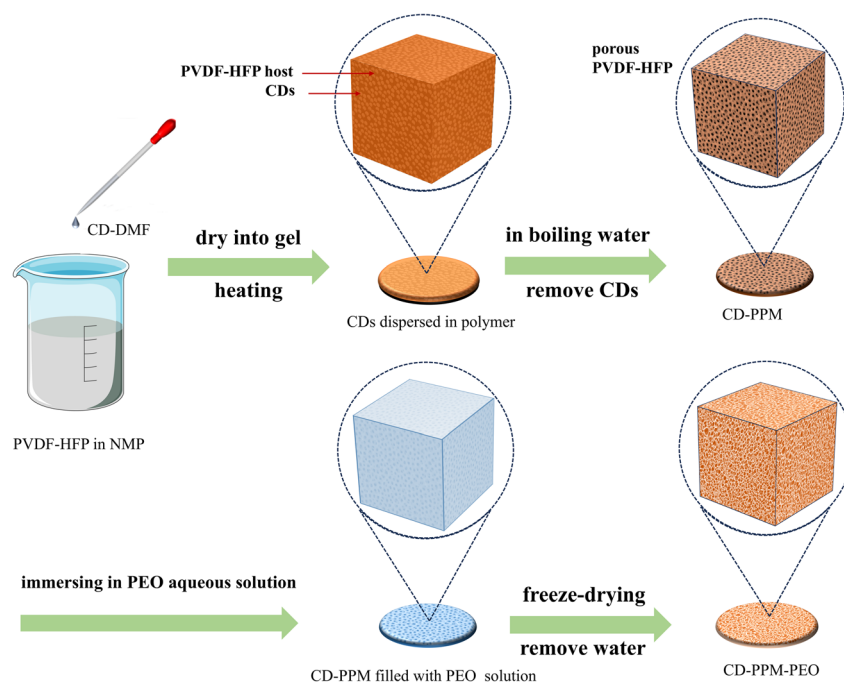


Fig. 1 Fabrication route of the porous CD-PPMs and the PEO-filled PEO-CD-PPM.



PEO into the pre-formed PVDF–HFP porous framework so as to avoid the direct mixing of PEO and PVDF–HFP in solutions. In this way, PEO aqueous solutions are added to PPM and CD-PPM films separately until saturation. The obtained gel-like membranes are freeze-dried to remove water, leaving PEO deposited in the pores of PVDF–HFP. During this process, the expansive ice crystals pierce the hole walls and connect the pores with the channel, which favors the subsequent LE absorption. The as-prepared samples are labelled as PEO-PPM and PEO-CD-PPM respectively.

### 3.2 Characterizing PEO-CD-PPM

Fig. 2a–f illustrate SEM images of PEO-PPM and PEO-CD-PPM samples prepared at different ratios. When no CDs are

involved, the resulting PEO-PPM has small and few pores (Fig. 2a). As the CDs ratio increases gradually, both the porosity and pore size increase in the PEO-CD-PPM samples (Fig. 2b–f). One of the samples was cut for cross-sectional imaging by SEM, the result shows the connected channels inside (Fig. 2g), which facilitates liquid electrolyte absorption and accelerates  $\text{Li}^+$  ion diffusion in GPEs.<sup>30,31</sup> Porosity data shown in Fig. 2h show that the porosity of PEO-PPM is only 32%, while the optimal porosity of PEO-CD-PPMs is over 70%. As a result, the LE uptake amount of PEO-PPM is about 200 wt%, while that of PEO-CD-PPM is close to 500 wt% (Fig. 2i), thus, the latter-derived GPEs have much higher conductivities.<sup>36</sup>

The DSC curves in Fig. S3† show the melting points of PVDF–HFP, PEO-PPM, and PEO-CD-PPM as 165.91 °C, 151.2 °C, and

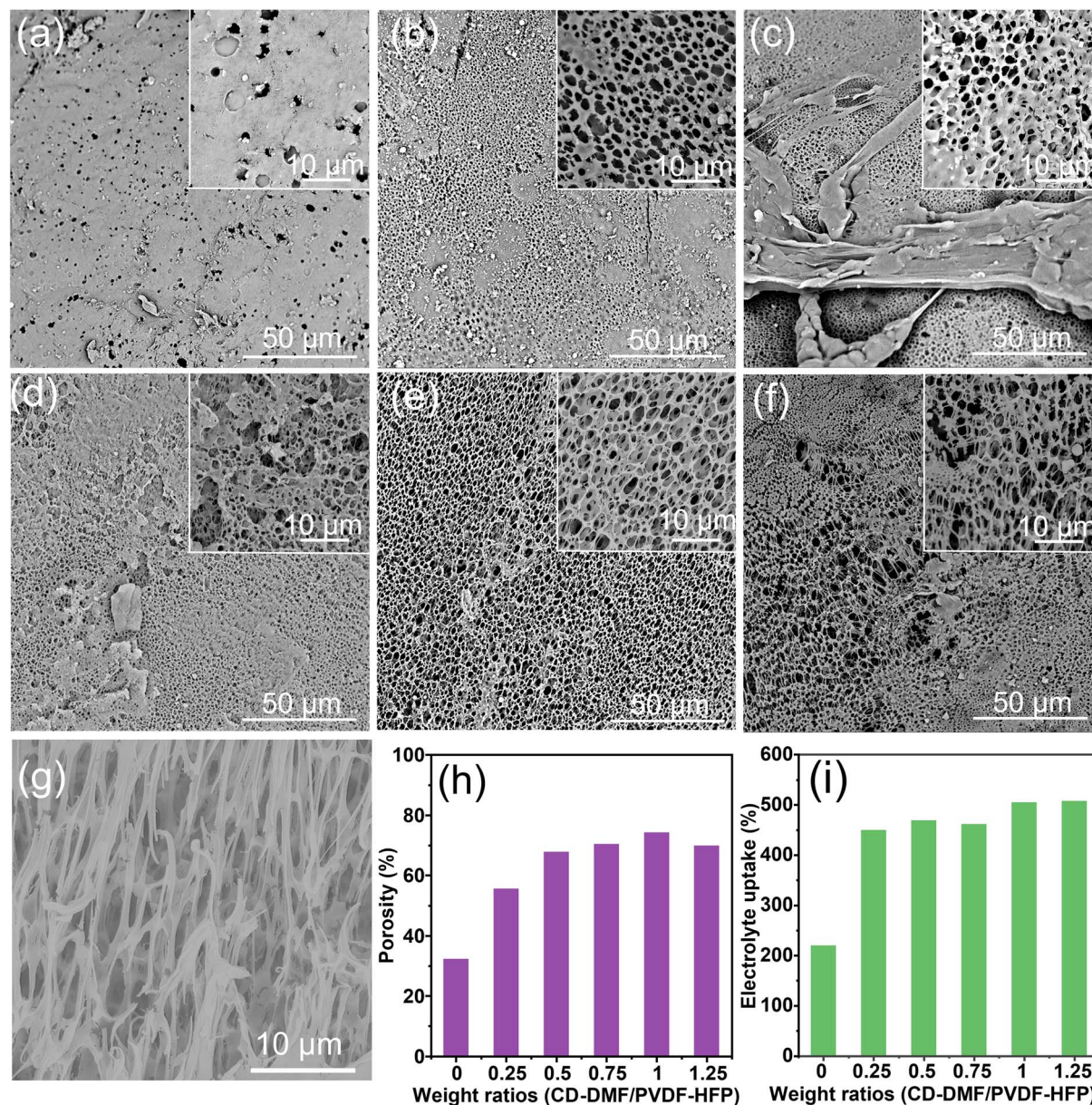


Fig. 2 SEM images of the CD-PPM samples prepared at different weight ratios of CD-DMF and PVDF–HFP: (a) 0, (b) 0.25, (c) 0.5, (d) 0.75, (e) 1.0 and (f) 1.25. (g) Cross-sectional SEM image of the sample (e). (h) Porosity of the above samples. (i) The LE uptake weight ratios (%) of the above samples after PEO deposition.

148.1 °C, respectively, which indicates that PEO incorporation decreases the melting point of PVDF–HFP on one hand, and on the other, PEO-CD-PPM has a higher content of PEO than PEO-PPM due to the larger porosity of CD-PPM. After absorbing LE, the resulting GPE(PEO-CD-PPM) and GPE(PEO-PPM) exhibit conductivities of  $3.8 \times 10^{-3} \text{ S cm}^{-1}$  and  $1.5 \times 10^{-4} \text{ S cm}^{-1}$  at room temperature, respectively. As shown in Fig. S3b,† CDs play a key role in making pores in PVDF–HFP, which enlarges the LE uptake in the resulting GPEs and finally improves the conductivities of the GPEs.<sup>37</sup> Moreover, there are a few CDs in CD-PPM-PEO, which can be proved from the fluorescence spectra in Fig. S4.† The intermolecular interaction among lithium salts, CDs, and PVDF–HFP can restrain the movement of the anions, and thus increase the ion transference numbers  $t_{\text{Li}^+}$ .<sup>38</sup> The  $t_{\text{Li}^+}$  were measured and calculated before and after polarization (Fig. S5†), demonstrating that the  $t_{\text{Li}^+}$  of GPE(PEO-CD-PPM) is up to 0.56, much higher than that 0.36 of GPE(PEO-PPM). The electrochemical stability windows (ESW) of the samples were measured by linear sweep voltammetry (LSV), which were 5 V for GPE(PEO-CD-PPM) (Fig. S5a†) and 4.9 V for GPE(PEO-PPM) (Fig. S5b†). The introduction of CDs widened the electrochemical window, which may be attributed to the shielding action of CDs on the hydroxyl groups at the ends of PEO.<sup>39,40</sup>

These GPEs were assembled into Li symmetric cells and measured by galvanostatic cycles to assess the electrolyte stability during the stripping/plating process at room

temperature. When the current density was set at  $0.5 \text{ mA cm}^{-2}$ , the voltage polarization of the Li||GPE(PEO-PPM)||Li cell was observed after 350 h of cycling, attributed to the “dead lithium” accumulation (Fig. 3a).<sup>41,42</sup> In contrast, the Li||GPE(PEO-CD-PPM)||Li cell tested under identical parameters demonstrated consistently minimal overpotential after 1000 h. It has been reported that a well-ordered porous structure in electrolytes can facilitate directed  $\text{Li}^+$  migration and uniform  $\text{Li}^+$  flux across the interface layer, thus contributing to optimal cyclic stability under high current densities.<sup>43</sup> To test this idea, a high current density of  $2.5 \text{ mA cm}^{-2}$  was applied to the Li||GPE(PEO-CD-PPM)||Li cell, which cycled steadily for over 3000 h (Fig. S7†). On the contrary, the Li||GPE(PEO-PPM)||Li cell did not work at all, indicating that the conductivity of GPE(PEO-PPM) was too low to support such a high current. At the above two current densities, the cell voltage of the Li||GPE(PEO-CD-PPM)||Li cells decreases significantly, which may be ascribed to the SEI formation and the improved electrode–electrolyte contact.<sup>44</sup> In contrast, the severe polarization of the Li||GPE(PEO-PPM)||Li cell is owing to the continuous SEI breakdown-reformation process, which produces plenty of “dead Li” and Li dendrites and finally destroys the cell. To study the influence of GPEs on Li electrodes, Li foils were dismantled from the cells after 100, 200, and 300 hours of cycling at a current density of  $0.5 \text{ mA cm}^{-2}$ , and observed under a scanning electron microscope (SEM). For the GPE(PEO-CD-PPM) contacted Li foils (Fig. 3b–d),

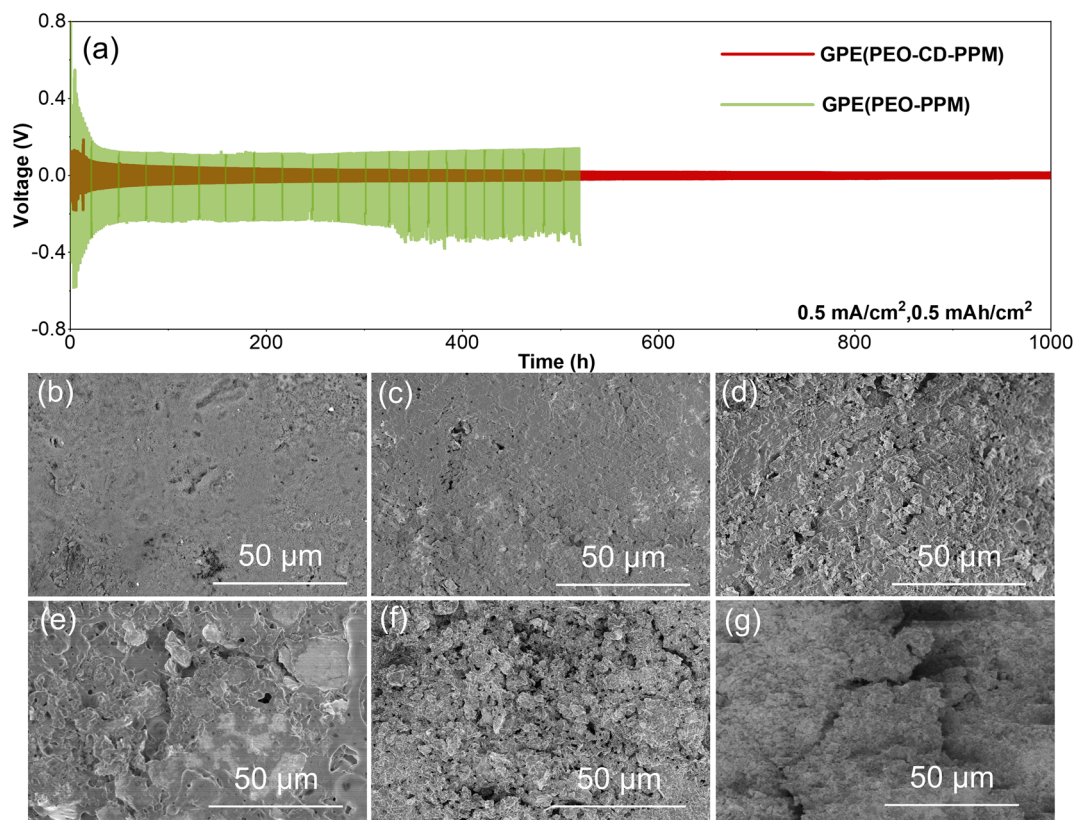


Fig. 3 (a) Galvanostatic cycling of Li||Li symmetric cells using GPE(PEO-CD-PPM) and GPE(PEO-PPM) at a current density of  $0.5 \text{ mA cm}^{-2}$  and an areal capacity of  $0.5 \text{ mA h cm}^{-2}$ . SEM images of Li foils dismantled from the Li||GPE(PEO-CD-PPM)||Li cells after cycling for (b) 100, (c) 200, and (d) 300 h. SEM images of Li foils dismantled from the Li||GPE(PEO-PPM)||Li cells after cycling for (e) 100, (f) 200, and (g) 300 h.



the surfaces are flat and dense, indicating that stable SEI films were formed to protect the Li surfaces. However, for the GPE(PEO-PPM) contacted Li foils, the surfaces are coarse and bumpy, with many holes in the foils. As the cycling time increases, the foil becomes more and more loose and porous (Fig. 3e–g), with pronounced moss-like dendrites, indicating that Li foils are corroded by electrochemical reactions and the SEI films undergo recurrent disintegration and reformation.<sup>45,46</sup>

X-ray photoelectron spectroscopy (XPS) was employed to analyze the chemical composition of the Li foil surface from the above symmetric cells after cycling (Fig. S8†). For the Li foil from Li||GPE(PEO-CD-PPM)||Li cells, C1s spectral analysis revealed the existence of C–C and C–O groups, owing to the decomposition of LEs and lithium salts. There also existed other decomposition products, such as C–F at about 686.6 eV, LiF at about 585.6 eV, and  $\text{Li}_x\text{PO}_y\text{F}_z$  bonds at about 687.4 eV.<sup>47</sup> In

addition, the presence of polyvinylidene fluoride (PVDF) chain was confirmed from the XPS peak at about 688.4 eV ( $-\text{CH}_2\text{CHF}-$ ). Such heterogeneous structures comprising multiple components are regarded to enhance ionic conductivities while diminishing Li anode electronic insulation.<sup>48,49</sup> LiF, recognized for its high mechanical modulus, can prevent lithium dendrite proliferation and impede interface side reactions,<sup>50</sup> although its substantial energy barrier may encumber  $\text{Li}^+$  migration.<sup>51</sup> This limitation can be improved by incorporating other ionic conductive constituents, hence enhancing the conductivity and mechanical properties of the SEI films rich in Li.<sup>50,52</sup> Inclusion of  $\text{Li}_x\text{PO}_y\text{F}_z$  is considered favorable for  $\text{Li}^+$  migration,<sup>53</sup> and the  $-\text{CH}_2\text{CHF}-$  from PVDF contributes to the formation of flexible polymeric layers supporting other products.<sup>54,55</sup> Stability of these decomposition products after 300 h corroborates the durability of SEI between Li foils and GPE(PEO-CD-PPM).

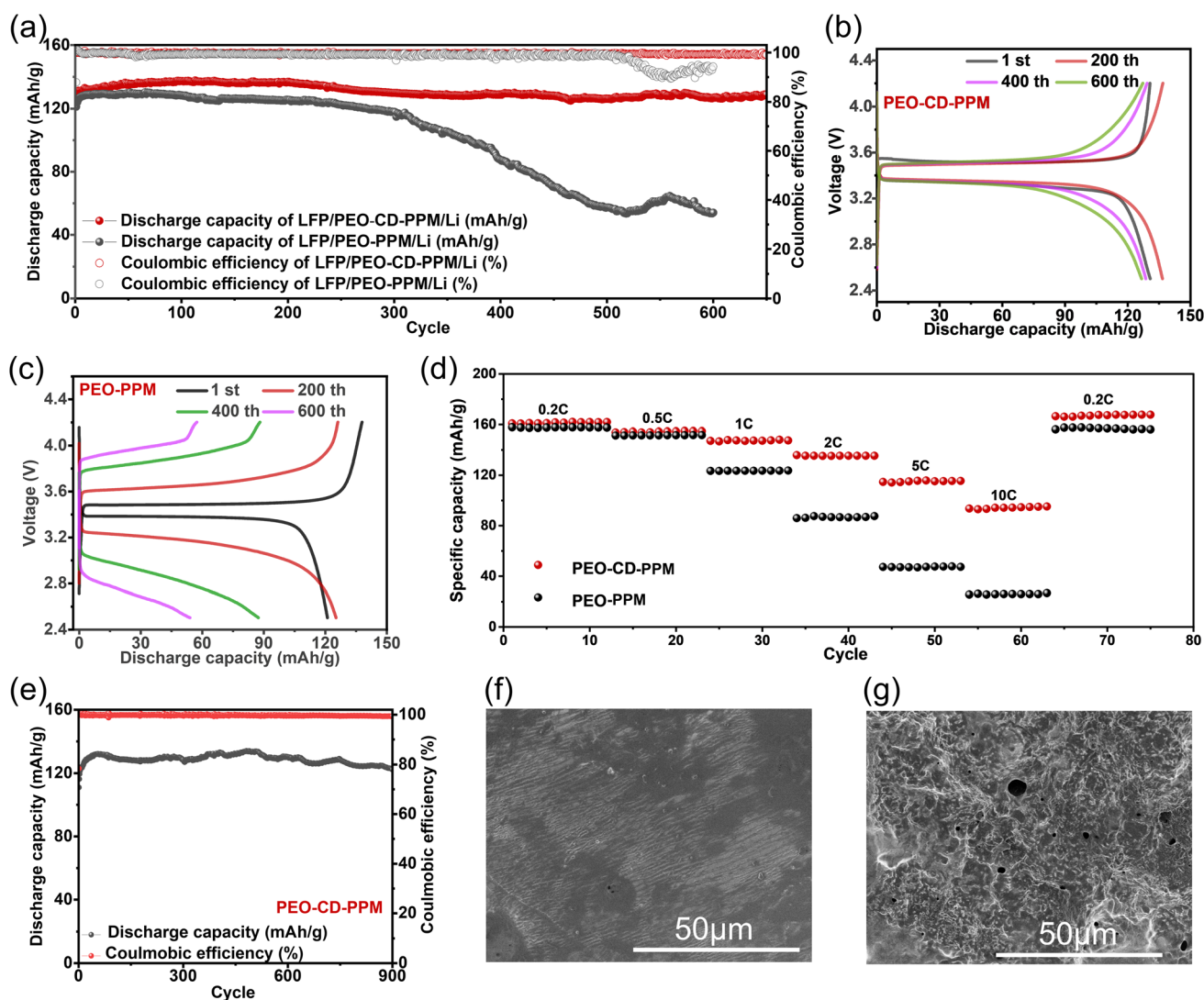


Fig. 4 (a) Discharge capacity and coulombic efficiency of Li||GPE||LiFePO<sub>4</sub> batteries cycled at 0.5C, using GPE(PEO-PPM) and GPE(PEO-CD-PPM) as electrolytes, respectively. Corresponding discharge capacities of (b) Li||GPE(PEO-CD-PPM)||LiFePO<sub>4</sub> and (c) Li||GPE(PEO-PPM)||LiFePO<sub>4</sub> at the 1st, 200th, 400th and 600th cycle. (d) The rate performance of Li||GPE(PEO-CD-PPM)||LiFePO<sub>4</sub> and Li||GPE(PEO-PPM)||LiFePO<sub>4</sub>. (e) Li||GPE(PEO-CD-PPM)||LiFePO<sub>4</sub> battery cycling performance at 1C. SEM images of the Li anode after 100 cycles at 5C from (f) Li||GPE(PEO-CD-PPM)||LiFePO<sub>4</sub> and (g) Li||GPE(PEO-PPM)||LiFePO<sub>4</sub>.

### 3.3 Application in Li||LiFePO<sub>4</sub> batteries

The electrochemical performances of Li||LiFePO<sub>4</sub> batteries with the above two GPEs were evaluated at a voltage range of 2.5–4.2 V at RT without temperature control. Initially, the Li||GPE(PEO-CD-PPM)||LiFePO<sub>4</sub> battery demonstrated a discharge capacity of 139.4 mA h g<sup>-1</sup> at a rate of 0.5C, and exhibited a coulombic efficiency approaching 100%. This efficiency is superior to that of Li||GPE(PEO-PPM)||LiFePO<sub>4</sub>, which yielded a capacity of 133.6 mA h g<sup>-1</sup> with a coulombic efficiency of 87.9% (Fig. 4a). Furthermore, Li||GPE(PEO-CD-PPM)||LiFePO<sub>4</sub> showed slowly enhanced specific capacities and improved the retention rates of capacity over multiple charge and discharge cycles. After 200 cycles, such improvements were significant. This phenomenon is owing to the gradually optimized interfaces between electrodes and the electrolyte during cycles, which make the whole active material (mainly the cathode) participate in the electrochemical reactions to release the maximum capacity. Its capacity retention was preserved at 98.58% and 97.47% after 400 and 600 cycles, respectively, indicating that Li||GPE(PEO-CD-PPM)||LiFePO<sub>4</sub> was very stable. As shown in Fig. 4b, the performance of Li||GPE(PEO-CD-PPM)||LiFePO<sub>4</sub> is good, while the charge and discharge curve polarization is serious and the capacity decay of Li||GPE(PEO-PPM)||LiFePO<sub>4</sub> shown in Fig. 4c is very fast. In the rate capability tests conducted at room temperature (Fig. 4d, here, 1C is defined as 170 mA g<sup>-1</sup>), the discharge capacities of Li||GPE(PEO-CD-PPM)||LiFePO<sub>4</sub> are measured as 161.6 mA h g<sup>-1</sup> at 0.2C, 154.5 mA h g<sup>-1</sup> at 0.5C, 147.8 mA h g<sup>-1</sup> at 1C, 135.4 mA h g<sup>-1</sup> at 2C, 115.4 mA h g<sup>-1</sup> at 5C, 94.2 mA h g<sup>-1</sup> at 10C. In contrast, the capacity of Li||GPE(PEO-PPM)||LiFePO<sub>4</sub> decays radically when cycling at a high rate. Specifically, when the rate increases to 10C, the capacity of Li||GPE(PEO-PPM)||LiFePO<sub>4</sub> is only 23.4 mA h g<sup>-1</sup>. In general, the cycling stability of a battery at elevated C-rates is critical for its practical applications. Li||GPE(PEO-CD-PPM)||LiFePO<sub>4</sub> is able to maintain a discharge capacity of 124.4 mA h g<sup>-1</sup> and a coulombic efficiency of nearly 100% at 1C after 900 cycles (Fig. 4e). Even working at 5C, it can still maintain a capacity of 87% and a coulombic efficiency of 99.6% after 1000 cycles (Fig. S9†). Li anodes were detached from the above LMBs and investigated by SEM. In Fig. 4f, the Li anode contacted with GPE(PEO-CD-PPM) after 100 cycles at 0.5C shows a dense and flat surface, while in Fig. 4g, the Li anode contacted with GPE(PEO-PPM) is porous and coarse. This is the direct proof of the superior cycling stability of Li||GPE(PEO-CD-PPM)||LiFePO<sub>4</sub>. To study the surface evolution of the Li anode over cycles, the Li foils were detached from the batteries after different cycles. Their SEM images shown in Fig. S10† indicate that some black patches grow gradually (after 10 cycles) until the coating of the Li surface is complete (after 150 cycles), which means a uniform and compact SEI was formed on the Li surface.

There are many kinds of pore-forming agents, such as small molecules, polymers, inorganic compounds, and nanoparticles, but most of them cannot be recycled, *i.e.*, these agents are usually removed by calcination or decomposition after the synthesis of porous materials. On the contrary, our CDs can be easily recycled for the next synthesis. These CDs are completely

dissolved by boiling water out of the polymer matrix and then dried for dissolution in DMF for a new preparation (Fig. S11†). The CD-PPM was prepared by the recycled CDs, and processed in the same route to fabricate Li||GPE(PEO-CD-PPM)||LiFePO<sub>4</sub> batteries, which were measured at different rates (Fig. S12†). At 0.5C, the battery sustained 500 cycles without any capacity attenuation and a coulombic efficiency of 99.62%. At 1C, the battery sustained 1000 cycles with a discharge capacity of 121.5 mA h g<sup>-1</sup> and a coulombic efficiency of 99.71%. These results confirm that the recovered CDs have the same pore-forming functions as the original ones, and thus this pore-forming agent possesses outstanding merits over its counterparts.

## 4 Conclusions

For the first time, carbon dots (CDs) were shown to serve as efficient pore-making agents in creating porous PVDF-HFP films with high porosity and electrolyte retention through solvent exchange and freeze-drying. After the PEO deposition and the electrolyte absorption, the obtained “polymer in polymer” GPEs possess superior ionic conductivity and Li-ion migration at room temperature. The LMBs assembled with such GPEs show robust stability across various C-rates during thousands of cycles, because they form a dense and stable SEI film on the surface of the Li anode, which hinders the dendrite growth and electrode corrosion. As a key role of the present research, CDs exhibit unique pore-creating ability with excellent sustainability and recyclability. This pore-making technique may be applied to fabricate other functional materials, such as catalyst carriers, gas adsorbents, liquid filters, soundproofing materials, and thermal insulation materials in the future.

## Data availability

The authors confirm that all relevant data supporting the findings of this study are available within the article and its ESI.†

## Conflicts of interest

The authors declare no conflict of interest.

## Acknowledgements

This study was financially supported by the National Natural Science Foundation of China (U24A20565, 21975048) and the Science and Technology Commission of Shanghai Municipality (2024ZDSYS02).

## References

- 1 J. W. Li, Z. Kong, X. X. Liu, B. C. Zheng, Q. H. Fan, E. Garratt, T. Schuelke, K. L. Wang, H. Xu and H. Jin, *InfoMat*, 2021, 3, 1333–1363.
- 2 Y. Han, B. Liu, Z. Xiao, W. Zhang, X. Wang, G. Pan, Y. Xia, X. Xia and J. Tu, *InfoMat*, 2021, 3, 155–174.
- 3 X. B. Cheng, R. Zhang, C. Z. Zhao, F. Wei, J. G. Zhang and Q. Zhang, *Adv. Sci.*, 2016, 3, 1500213.

- 4 S. Li, J. Huang, Y. Cui, S. Liu, Z. Chen, W. Huang, C. Li, R. Liu, R. Fu and D. Wu, *Nat. Nanotechnol.*, 2022, **17**, 613.
- 5 Y.-F. Huang, T. Gu, G. Rui, P. Shi, W. Fu, L. Chen, X. Liu, J. Zeng, B. Kang, Z. Yan, F. J. Stadler, L. Zhu, F. Kang and Y.-B. He, *Energy Environ. Sci.*, 2021, **14**, 6021–6029.
- 6 B. Qiu, F. Xu, J. Qiu, M. Yang, G. Zhang, C. He, P. Zhang, H. Mi and J. Ma, *Energy Storage Mater.*, 2023, **60**, 102832.
- 7 B. Huang, Z. H. Li, Y. M. Zhu, Y. Che and C. A. Wang, *Rare Met.*, 2022, **41**, 2826–2833.
- 8 J. Sang, B. Tang, K. Pan, Y. B. He and Z. Zhou, *Acc. Mater. Res.*, 2023, **4**, 472–483.
- 9 Z. Li, J. Fu, X. Zhou, S. Gui, L. Wei, H. Yang, H. Li and X. Guo, *Adv. Sci.*, 2023, **10**, 2505.
- 10 S. Fu, L. L. Zuo, P. S. Zhou, X. J. Liu, Q. Ma, M. J. Chen, J. P. Yue, X. W. Wu and Q. Deng, *Mater. Chem. Front.*, 2021, **5**, 5211–5232.
- 11 L. Gao, B. Tang, H. Jiang, Z. Xie, J. Wei and Z. Zhou, *Adv. Sustainable Syst.*, 2022, **6**, 2100389.
- 12 X. Pei, Y. Li, T. Ou, X. Liang, Y. Yang, E. Jia, Y. Tan and S. Guo, *Angew. Chem., Int. Ed.*, 2022, **61**, 2205075.
- 13 W. Ren, C. Ding, X. Fu and Y. Huang, *Energy Storage Mater.*, 2021, **34**, 515–535.
- 14 J. I. Kim, Y. Choi, K. Y. Chung and J. H. Park, *Adv. Funct. Mater.*, 2017, **27**, 1701768.
- 15 X. Liu, O. O. Taiwo, C. Yin, M. Ouyang, R. Chowdhury, B. Wang, H. Wang, B. Wu, N. P. Brandon, Q. Wang and S. J. Cooper, *Adv. Sci.*, 2019, **6**, 1801337.
- 16 J. Y. Wan, J. Xie, X. Kong, Z. Liu, K. Liu, F. F. Shi, A. Pei, H. Chen, W. Chen, J. Chen, X. K. L. Q. Zong, J. Y. Wang, L. Q. Chen, J. Qin and Y. Cui, *Nat. Nanotechnol.*, 2019, **14**, 705.
- 17 S. Liu, L. Zhou, J. Han, K. Wen, S. Guan, C. Xue, Z. Zhang, B. Xu, Y. Lin, Y. Shen, L. Li and C. W. Nan, *Adv. Energy Mater.*, 2022, **12**, 2200660.
- 18 J. Gou, Z. Zhang, S. Wang, J. Huang, K. Cui and H. Wang, *Adv. Mater.*, 2023, 23096777.
- 19 W. Ling, N. Fu, J. P. Yue, X. X. Zeng, Q. Ma, Q. Deng, Y. Xiao, L. J. Wan, Y. G. Guo and X. W. Wu, *Adv. Energy Mater.*, 2020, **10**, 1903966.
- 20 J. Y. Xi, X. P. Qiu and L. Q. Chen, *Solid State Ionics*, 2006, **177**, 709–713.
- 21 H. X. He, Y. M. Fu, T. M. Zhao, X. C. Gao, L. L. Xing, Y. Zhang and X. Y. Xue, *Nano Energy*, 2017, **39**, 590–600.
- 22 H. Ding, S. B. Yu, J. S. Wei and H. M. Xiong, *ACS Nano*, 2016, **10**, 484–491.
- 23 L. Vallan, E. P. Urriolabeitia, F. Ruiperez, J. M. Matxain, R. Canton-Vitoria, N. Tagmatarchis, A. M. Benito and W. K. Maser, *J. Am. Chem. Soc.*, 2018, **140**, 12862–12869.
- 24 J. S. Wei, C. Ding, P. Zhang, H. Ding, X. Q. Niu, Y. Y. Ma, C. Li, Y. G. Wang and H. M. Xiong, *Adv. Mater.*, 2019, **31**, 1806197.
- 25 T. B. Song, Z. H. Huang, X. R. Zhang, J. W. Ni and H. M. Xiong, *Small*, 2023, **19**, 2205558.
- 26 X. Zhao, J. S. Wei, T. B. Song, Z. R. Wang, D. W. Yang, X. R. Zhang, F. Huo, Y. Q. Zhang and H. M. Xiong, *Chem. Eng. J.*, 2024, **481**, 148779.
- 27 W. Liu, T. Xie, X. Wang, W. Deng, L. Huang, R. Khan, Y. Wang, H. Hou, D. Wang and Y. Wu, *Adv. Funct. Mater.*, 2024, **8**, 241083.
- 28 C. Ma, K. Dai, H. Hou, X. Ji, L. Chen, D. C. Ivey and W. Wei, *Adv. Sci.*, 2018, **5**, 1700996.
- 29 C. Li, L. Ou, Y. Liu, L. Xu, S. Zhou, L. Guo, H. Liu, Z. Zhang, M. Cui, G. Chen, J. Huang and J. Tao, *Adv. Mater. Technol.*, 2023, **8**, 2202002.
- 30 H. Ding, S.-B. Yu, J.-S. Wei and H.-M. Xiong, *ACS Nano*, 2016, **10**, 484–491.
- 31 S. N. Qu, X. Y. Wang, Q. P. Lu, X. Y. Liu and L. J. Wang, *Angew. Chem., Int. Ed.*, 2012, **51**, 12215–12218.
- 32 Z. Mou, B. Zhao, B. Wang and D. Xiao, *ACS Appl. Mater. Interfaces*, 2021, **13**, 8794–8807.
- 33 X. Xu, L. Mo, Y. Li, X. Pan, G. Hu, B. Lei, X. Zhang, M. Zheng, J. Zhuang, Y. Liu and C. Hu, *Adv. Mater.*, 2021, **33**, 2104872.
- 34 G. H. Chen, F. Zhang, Z. M. Zhou, J. R. Li and Y. B. Tang, *Adv. Energy Mater.*, 2018, **8**, 1801219.
- 35 P. Xu, H. Chen, X. Zhou and H. Xiang, *J. Membr. Sci.*, 2021, **617**, 118660.
- 36 C. Yang, Y. Bai, H. Xu, M. Li, Z. Cong, H. Li, W. Chen, B. Zhao and X. Han, *Polymers*, 2022, **14**, 1181.
- 37 L. Xu, X. Xiao, H. Tu, F. Zhu, J. Wang, H. Liu, W. Huang, W. Deng, H. Hou, T. Liu, X. Ji, K. Amine and G. Zou, *Adv. Mater.*, 2023, **35**, 2303193.
- 38 L. Xu, H. Tu, F. Zhu, Y. Xiang, Z. Luo, S. Fang, W. Deng, G. Zou, H. Hou and X. Ji, *SmartMat*, 2022, **3**, 286–297.
- 39 H. Liu, Y. Ye, F. Zhu, X. Zhong, D. Luo, Y. Zhang, W. Deng, G. Zou, H. Hou and X. Ji, *Angew. Chem., Int. Ed.*, 2024, **63**, e202409044.
- 40 X. F. Yang, M. Jiang, X. J. Gao, D. Bao, Q. Sun, N. Holmes, H. Duan, S. Mukherjee, K. Adair, C. T. Zhao, J. W. Liang, W. H. Li, J. J. Li, Y. Liu, H. Huang, L. Zhang, S. G. Lu, Q. W. Lu, R. Y. Li, C. V. Singh and X. L. Sun, *Energy Environ. Sci.*, 2020, **13**, 1318–1325.
- 41 G. Y. Zheng, S. W. Lee, Z. Liang, H. W. Lee, K. Yan, H. B. Yao, H. T. Wang, W. Y. Li, S. Chu and Y. Cui, *Nat. Nanotechnol.*, 2014, **9**, 618–623.
- 42 X. Li, J. Liu, J. He, S. Qi, M. Wu, H. Wang, G. Jiang, J. Huang, D. Wu, F. Li and J. Ma, *Adv. Sci.*, 2022, **12**, 2201297.
- 43 L. Yue, X. Wang, C. Li, D. Shen, Z. Shao, H. Wu, s. xiao, W. Liang, Y. Yu and Y. Li, *Energy Environ. Sci.*, 2024, **17**, 1117–1131.
- 44 J. B. Park, C. Choi, S. Yu, K. Y. Chung and D.-W. Kim, *Adv. Energy Mater.*, 2021, **11**, 2101544.
- 45 H. Jia, C. Zeng, H.-S. Lim, A. Simmons, Y. Zhang, M. H. Weber, M. H. Engelhard, P. Gao, C. Niu, Z. Xu, J.-G. Zhang and W. Xu, *Adv. Mater.*, 2023, **11**, e2311312.
- 46 T. Yi, E. Zhao, Y. He, T. Liang and H. Wang, *eScience*, 2024, **4**, 100182.
- 47 Z. H. Huang, J. S. Wei, T. B. Song, J. W. Ni, F. Wang and H. M. Xiong, *SmartMat*, 2022, **3**, 323–336.
- 48 J. Tan, J. Matz, P. Dong, J. F. Shen and M. X. Ye, *Adv. Energy Mater.*, 2021, **11**, 2100046.
- 49 S. M. Li, J. L. Huang, Y. Cui, S. H. Liu, Z. R. Chen, W. Huang, C. F. Li, R. L. Liu, R. W. Fu and D. C. Wu, *Nat. Nanotechnol.*, 2022, **17**, 613.



- 50 J. Yang, J. Hou, Z. Fang, K. Kashif, C. Chen, X. Li, H. Zhou, S. Zhang, T. Feng, Z. Xu and M. Wu, *Chem. Eng. J.*, 2022, **433**, 113193.
- 51 X. B. Cheng, C. Yan, X.-Q. Zhang, H. Liu and Q. Zhang, *ACS Energy Lett.*, 2018, **3**, 1564–1570.
- 52 A. Hu, W. Chen, X. Du, Y. Hu, T. Lei, H. Wang, L. Xue, Y. Li, H. Sun, Y. Yan, J. Long, C. Shu, J. Zhu, B. Li, X. Wang and J. Xiong, *Energy Environ. Sci.*, 2021, **14**, 4115–4124.
- 53 Y. Wang, H. Zheng, L. Hong, F. Jiang, Y. Liu, X. Feng, R. Zhou, Y. Sun and H. Xiang, *Chem. Eng. J.*, 2022, **445**, 136802.
- 54 W. Y. Liu, C. J. Yi, L. P. Li, S. L. Liu, Q. Y. Gui, D. L. Ba, Y. Y. Li, D. L. Peng and J. P. Liu, *Angew. Chem., Int. Ed.*, 2021, **60**, 12931–12940.
- 55 J. Luo, C. C. Fang and N. L. Wu, *Adv. Energy Mater.*, 2018, **8**, 1701482.